Neutron diffraction study on dynamic compression deformation behavior of GH4738 nickel-based superalloy*

LI Hongjia, XIA Shangwu, XIE Lei, FAN Zhijian

National Key Laboratory of Neutron Science and Technology, Institute of Nuclear Physics and Chemistry, China Academy of Engineering Physics, Mianyang 621999, China

Abstract Nickel-based superalloys are widely used in aero-engines due to their high strength, toughness, corrosion resistance, and creep resistance at elevated temperatures. Strain rate, temperature, and strain are critical factors influencing the microstructural evolution of nickel-based superalloys. This study investigates the dynamic compressive deformation behavior of GH4738, a typical nickel-based superalloy. SHPB compression tests were performed on the GH4738 superalloy at strain rates of 1000-7500 s^{-1} over a temperature range from room temperature (RT) to 500 ℃. The yield strength of the GH4738 superalloy decreases with increasing temperature and increases with increasing strain rate. However, it drops sharply at 500 ℃ and a strain rate of 7500 s^{-1}. To elucidate the microscopic deformation behavior, parallel specimens were prepared using the SHPB technique at frozen strains of -0.02, -0.05, -0.10, -0.20, and -0.25. These tests were conducted at a strain rate of 3000 s^{-1} for RT, 400 ℃, and 500 ℃. Neutron diffraction was employed to characterize the evolutions of lattice constants and elastic lattice strains. We define the horizontal lattice mismatch as the lattice misfit at the γ/γ' interface perpendicular to the SHPB compression direction. The vertical lattice mismatch is defined as the lattice misfit parallel to the SHPB compression direction. As the frozen strain increases, the horizontal lattice mismatch exhibits a positive value and an upward trend. In contrast, the vertical lattice mismatch shifts from positive to negative. The elastic lattice strain of the γ' phase continues to increase, whereas that of the γ phase remains nearly constant. The lattice strains of the {111} and {220} planes are negative at 400 ℃ and 500 ℃, respectively, but positive at RT. The lattice strain of the {200} plane alternates between positive and negative values from RT to 500 ℃. Meanwhile, the {311} plane strain remains negative throughout this temperature range. However, at a frozen strain of -0.25, the lattice strain of the {311} plane shows a significant rebound at both RT and 500 ℃. This indicates

* The paper is an English translated version of the original Chinese paper published in Acta Physica Sinica. Please cite the paper as: LI Hongjia, XIA Shangwu, XIE Lei, FAN Zhijian, **Neutron diffraction study on dynamic compression deformation behavior of GH4738 nickel-based superalloy.** *Acta Phys. Sin.*, 2026, 75(5): 050808. DOI: 10.7498/aps.75.20251510

the generation of substantial intergranular stresses within the material. TEM was used to characterize dislocation configurations and explain the underlying mechanisms. At RT, plastic deformation is dominated by γ-γ' co-deformation. Defects manifest as parallel slip bands and stacking faults. The formation of dislocation networks at γ/γ' interfaces effectively relaxes lattice misfit. Consequently, residual lattice strain at RT is minimal. At 500 ℃, dislocation density increases substantially because both γ and γ' phases readily undergo plastic deformation under thermal activation. Under these conditions, dislocation networks fail to compensate for lattice distortions caused by defect multiplication. This results in high lattice misfit and residual lattice strain. At 400 ℃, the alternating dominance of dislocation climb and slip induces fluctuations in both lattice misfit and residual lattice strain. Due to the slow accumulation of dislocation density, $\{hkl\}$ lattice strains continuously increase. This contrasts with the RT and 500 ℃ scenarios. In those cases, rising dislocation density partially recovers elastic lattice distortion. It even induces a rebound in $\{hkl\}$ lattice strain at high strains (ε = -0.20 to -0.25).

Keywords nickel-based superalloy; split Hopkinson pressure bar test; neutron diffraction; residual stress

doi: 10.7498/aps.74.20251510
cstr: 32037.14.aps.74.20251510

1 Introduction

Precipitation-strengthened nickel-based superalloys are widely used in hot-section components of aero-engines due to their combination of high strength, high toughness, corrosion resistance, and high-temperature creep resistance[1,2]. Evaluating the service performance, predicting the lifespan, and analyzing impact accidents of aero-engines require data on the dynamic failure processes of these materials. In nickel-based superalloys, the γ matrix phase has a face-centered cubic (FCC) structure, while the γ' precipitate phase has an $L1_2$ structure. The volume fraction of the γ' phase ranges from 20% to 50%[3-5]. Under external thermo-mechanical coupling, the thermal and elastoplastic anisotropy of nickel-based superalloys causes stress redistribution between adjacent grains and coherent γ-γ' phases, leading to structural and defect evolution[6,7]. Therefore, accurately obtaining the correlation between macroscopic properties and microscopic processes in nickel-based superalloys at high strain rates, as well as their evolution with temperature, holds significant scientific and practical value. Neutron diffraction is a key technique for determining material structures and internal strain/stress[8]. Due to the centimeter-scale penetration depth of neutrons, this technique can measure internal microstructures and three-dimensional residual strains, thereby accurately characterizing the anisotropic features of crystalline materials. Neutron diffraction enables multi-scale measurements of microstructural and mechanical parameters in superalloys, including aging phase structures[9,10], lattice misfit[11,12], dislocation evolution[3,13,14], strain/stress distribution[15-18], and texture component evolution[19]. However, research on the plastic deformation behavior of nickel-based superalloys under high strain rates currently focuses mainly on microstructural observation[20-22], theoretical model construction[23,24], and analysis of plastic deformation mechanisms based on electron backscattered diffraction (EBSD)[25]. There are no reports using neutron diffraction to study the dynamic deformation behavior of nickel-based superalloys.

This study investigates a typical nickel-based superalloy, GH4738, using neutron diffraction. We examined parallel specimens with a strain rate of 3000 s^{-1} and frozen strains of -0.02, -0.05, -0.10, -0.20, and -0.25. The tests were conducted under conditions ranging from room temperature (RT) to 500 ℃. We analyzed the anisotropic characteristics of lattice constants, lattice misfit, intergranular strain, and phase-average strain. Transmission electron microscopy (TEM) was used to characterize defect states, revealing the correspondence between microstructural and defect evolution and microscopic strain/stress states. This work provides important micro- and meso-scale data support for a comprehensive understanding of the dynamic deformation damage mechanisms in nickel-based superalloys.

2 Experimental

2.1 Sample Preparation

The experiment used GH4738 alloy[3]. Its chemical composition (wt%) is 16.81 Cr, 12.91 Co, 4.91 Mo, 2.63 Ti, 1.35 Si, 0.93 Al, 0.78 C, 0.51 Fe, less than 0.5% Ta, W, Cu, and other elements, with Ni as the balance. The alloy contains both secondary and tertiary γ' precipitates for strengthening. Their average grain sizes are (110 ± 25) nm and (16 ±2) nm, respectively. The volume fraction of the γ' precipitate phase, measured by full-spectrum neutron diffraction, is 30%. The volume fractions of the secondary and tertiary γ' precipitates are 10% and 20%, respectively. Compression samples were prepared using wire electrical discharge machining, with dimensions referencing the ASTM E8-04 standard. The samples are cylindrical, with a diameter of 4 mm and a height of 3.2 mm.

2.2 Dynamic Impact Experiment

The split Hopkinson pressure bar (SHPB) is widely used for dynamic experiments on engineering materials such as metals, composites, and ceramics in the strain rate range of 10^2-10^4 s^{-1}. The SHPB system used in this study has a bar diameter of 12.7 mm. The striker bar is 300 mm long, and both the incident and transmission bars are 1000 mm long. All bars are made of spring steel. The sample is placed between the incident and transmission bars. Vaseline is applied uniformly to the interfaces to reduce end-face friction. Tests were conducted at RT, 400 ℃, and 500 ℃, with strain rates of 1000, 3000, 5000, and 7500 s^{-1}, to obtain the dynamic compression mechanical curves of the GH4738 alloy. Furthermore, series of strain-frozen parallel specimens were prepared using the SHPB at a strain rate of 3000 s^{-1} and temperatures of RT, 400 ℃, and 500 ℃. The frozen strains were -0.02, -0.05, -0.10, -0.20, and -0.25, as shown in Fig. 1.

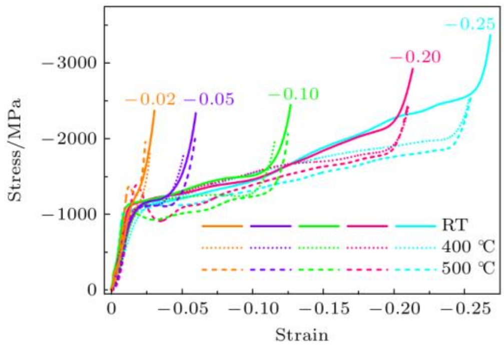

Fig. 1 Stress-strain curves of SHPB strain-frozen specimens of GH4738 superalloy at a strain rate of 3000 s^{-1} at RT, 400 ℃, and 500 ℃.

2.3 Neutron Diffraction Experiments

We conducted full-pattern neutron diffraction measurements using the High Pressure Neutron Diffractometer (HPND) at the China Mianyang Research Reactor (CMRR)[26]. The maximum neutron flux at the sample position is 2.8×10^6 n cm^{-2} s^{-1}. The detector array comprises 70 ^{3}He tubes, and we acquired data using a superimposed scanning mode. Based on the instrumental geometry, the diffraction vector $\boldsymbol{Q}$ remains perpendicular to the SHPB compression direction during full-pattern measurements. The sample rotates continuously, ensuring the entire cylindrical specimen is immersed within the neutron gauge volume, as shown in Figure 2(a). We set the acquisition time for each full-pattern scan to 2 h to obtain effective signals from the γ' phase. We performed lattice strain measurements for $\{hkl\}$ planes using the Residual Stress Neutron Diffractometer (RSND) at CMRR[27]. This instrument provides a maximum neutron flux of 4.7×10^6 n cm^{-2} s^{-1} at the sample position and a strain resolution of $\Delta d/d \leq 0.25\%$. The equipped sample stage supports a load of 500 kg, with a vertical travel of 0.5 m and a horizontal translation of ±0.3 m. In this study, we measured lattice strains for four crystallographic planes: {111}, {200}, {220}, and {311}. Due to the flexible diffraction geometry of the RSND, we directly measured lattice strains along the loading direction. Specifically, the diffraction vector $\boldsymbol{Q}$ was aligned parallel to the

SHPB compression direction, as illustrated in Figure 2(b). The acquisition time for the diffraction pattern of each plane ranged from 5 to 10 min.

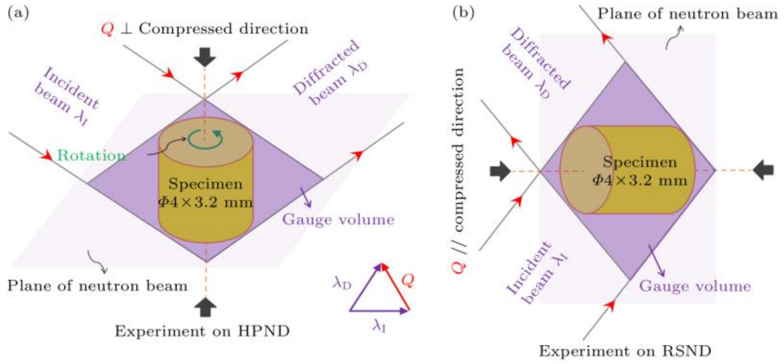

Fig. 2 Schematic diagrams of the relative position between neutron beam and specimen in neutron diffraction experiments: (a) HPND experiment; (b) RSND experiment.

3 Results and Discussion

3.1 Dynamic Mechanical Properties

Figures 3(a)-(c) present the compressive stress-strain curves of the GH4738 alloy at temperatures ranging from RT to 500 ℃ and strain rates between 1000 and 7500 s^{-1}. Figure 3(d) illustrates the evolution of yield strength with temperature. The hardening behavior of the GH4738 alloy remains similar across strain rates of 1000-7500 s^{-1} at RT, 400 ℃, and 500 ℃. Accounting for error factors such as SHPB dynamic impact wave fluctuations, the yield strength of the GH4738 alloy decreases with increasing temperature within the RT-500 ℃ range. Conversely, the yield strength increases with higher strain rates within the 1000-7500 s^{-1} range. However, a significant drop in yield strength occurs at 500 ℃ under a strain rate of 7500 s^{-1}. Furthermore, a comparison of Figures 3(b) and (c) reveals that the elongation at 500 ℃ is significantly lower than that at 400 ℃ when the strain rate is 7500 s^{-1}. The sharp decline in both yield strength and elongation under these conditions (500 ℃, 7500 s^{-1}) may be attributed to temperature-assisted slip. Additionally, increased plastic deformation mechanisms within the γ' phase at 500 ℃ likely accelerate plastic deformation and failure processes[28]. The defect characteristics discussed in Section 3.4 support this interpretation. Samples tend to fragment at large strains under strain rates of 5000 s^{-1} and 7500 s^{-1}. This fragmentation prevents the preparation of serial frozen specimens for neutron diffraction experiments. Therefore, this study selects a strain rate of 3000 s^{-1} as the representative high-speed impact rate. We investigate the evolution of microstructure, stress, and defect states with temperature to elucidate the dynamic impact deformation mechanism of the GH4738 alloy.

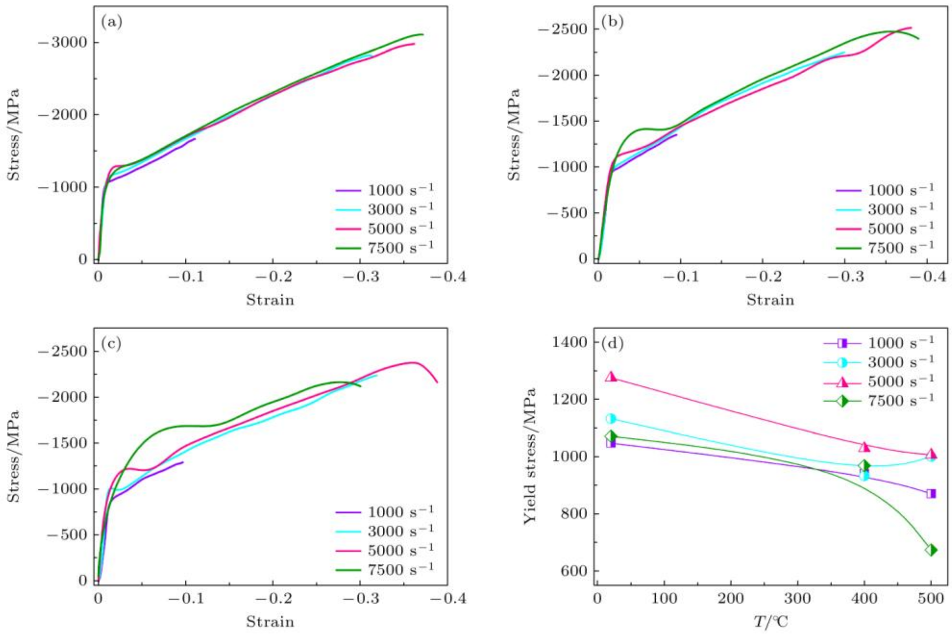

Fig. 3 Compressive stress-strain curves and yield strength of GH4738 superalloy at strain rates of 1000-7500 s^{-1}: (a) RT; (b) 400 ℃; (c) 500 ℃; (d) evolution of yield strength.

3.2 Lattice Mismatch

The HPND diffractometer measured full neutron diffraction patterns for samples with frozen strains of -0.05, -0.10, and -0.25, as well as for undeformed samples. These measurements were conducted at a strain rate of 3000 s^{-1} and temperatures ranging from RT to 500 ℃. Figure 4 presents the results. We applied full-pattern fitting and refinement methods[29,30] to determine the lattice constants of the GH4738 alloy under these experimental conditions. Figure 5(b) displays these results. Based on the HPND diffraction geometry shown in Figure 2(a), the directly measured lattice constant corresponds to the horizontal lattice constant. As defined in Figure 5(a), the horizontal lattice constant is perpendicular to the compression direction, while the vertical lattice constant is parallel to it. Under compressive impact loading, the horizontal lattice constant of the γ' phase increases with load. In contrast, the lattice constant of the γ phase remains nearly constant as the load increases. We can further calculate the lattice mismatch from these lattice constants. The γ-γ' lattice mismatch in nickel-based superalloys is defined as

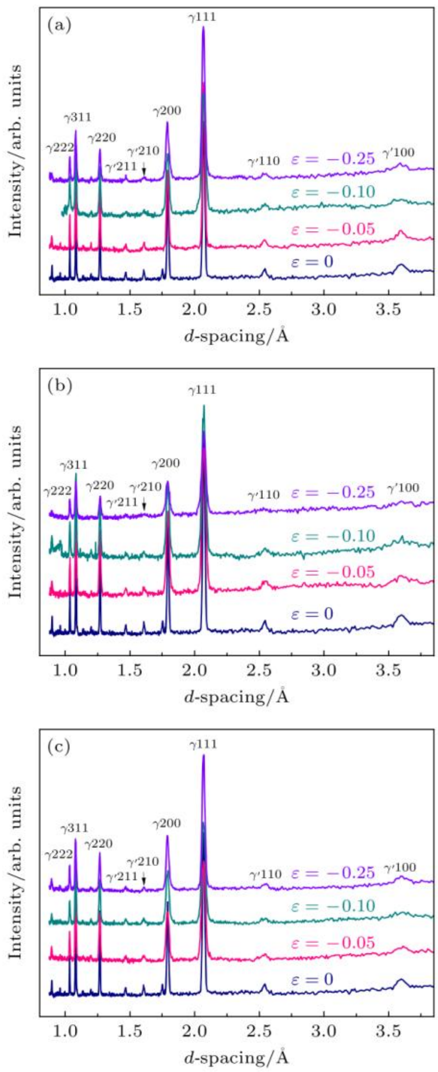

Fig. 4 Neutron diffraction patterns of GH4738 superalloy deformed at a strain rate of 3000 s^{-1} to frozen strains of -0.05, -0.10, and -0.25, along with the undeformed state, measured by HPND: (a) RT; (b) 400 ℃; (c) 500 ℃.

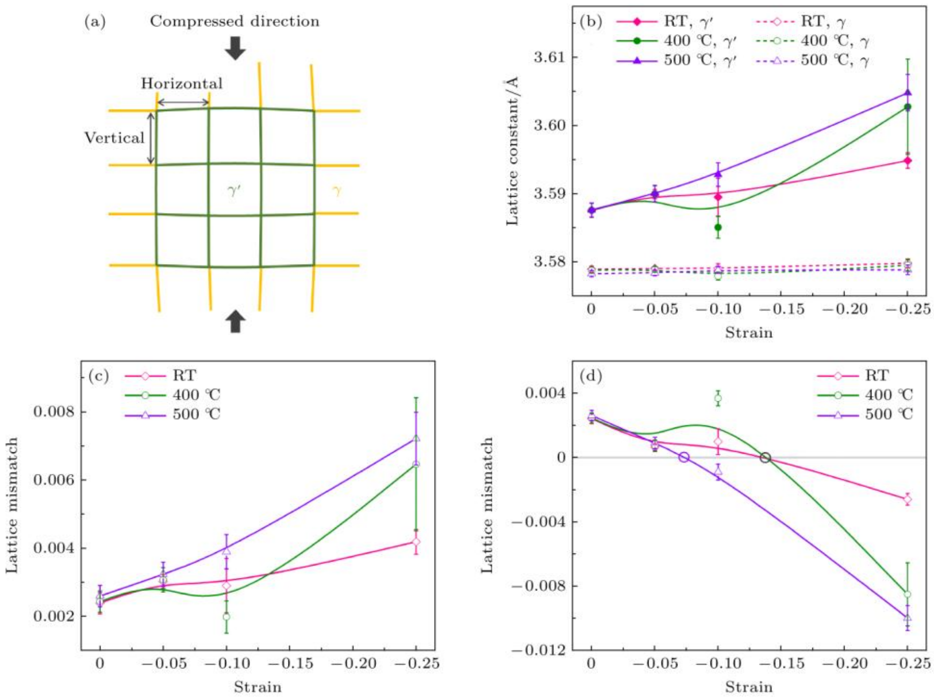

Fig. 5 Lattice constants and lattice mismatch derived from total diffraction pattern refinement: (a) Schematic of *γ*-*γ′* lattice mismatch; (b) horizontal lattice constants; (c) horizontal lattice mismatch; (d) vertical lattice mismatch.

$$\delta = 2\frac{a_{\gamma'} - a_{\gamma}}{a_{\gamma'} + a_{\gamma}}, \quad (1)$$

Here, δ denotes the lattice misfit, while $a_{\gamma'}$ and a_{γ} represent the lattice constants of the γ' and γ phases, respectively. Figure 5(c) illustrates the horizontal lattice misfit derived from horizontal lattice constants. At 500 ℃, the horizontal lattice misfit reaches its maximum and increases continuously with deformation. At 400 ℃, the horizontal lattice misfit decreases when the compressive strain ranges from -0.05 to -0.1, after which it continues to increase. At room temperature (RT), the horizontal lattice misfit is minimal and exhibits the smallest increase. The vertical lattice misfit is calculated using the following formula:

$$\varepsilon_{//} = -\frac{1}{\nu}\frac{a_{//} - a_0}{a_0}, \quad (2)$$

$$a_{\perp} = (1 + \varepsilon_{//})a_0, \quad (3)$$

In the equation, $\varepsilon_{//}$ denotes the lattice strain parallel to the compression direction. a_0 represents the lattice constant in the stress-free state. $a_{//}$ and $a_{\perp}$ denote the lattice constants parallel and perpendicular to the compression direction, respectively. ν is Poisson's ratio. The GH4738 alloy used in this study resembles the 720 Li alloy[5], as both feature a mixed γ' size microstructure. We calculated the average Poisson's ratio using the elastic modulus of the 720 Li alloy at RT-500 ℃ from the literature. The Poisson's ratios at RT, 400 ℃, and 500 ℃ are 0.36, 0.37, and 0.37, respectively. After obtaining the perpendicular lattice parameters from Eqs. (2) and (3), we calculated the perpendicular lattice misfit using Eq. (1). The results are shown in Fig. 5(d). At RT, 400 ℃, and 500 ℃, the perpendicular lattice misfit transitions from positive to negative as deformation increases. The strain values at these transition points are -0.14, -0.14, and -0.07, respectively. The negative misfit appears earliest at 500 ℃, indicating that the GH4738 alloy undergoes the greatest deformation damage under this condition.

3.3 Microscopic Strain Evolution

To investigate the microscopic deformation process of the GH4738 alloy, we performed neutron diffraction strain measurements on parallel samples with frozen strains of 0, -0.02, -0.05, -0.10, -0.20, and -0.25. To visually describe the evolution of lattice strain, we converted the frozen strains into stresses for plotting. Based on the SHPB stress-strain curves in Fig. 3(a)-(c), the stresses corresponding to the frozen strains at RT, 400 ℃, and 500 ℃ are (0, -1190, -1349, -1675, -2272, -2538) MPa, (0, -1000, -1162, -1441, -1914, -2096) MPa, and (0, -994, -1139, -1407, -1780, -1968) MPa, respectively. The results are presented in Fig. 6. After SHPB compression, the lattice strains of the {111}, {200}, and {220} planes exhibit consistent trends at RT-500 ℃, as shown in Fig. 6(a). Specifically, the lattice strains of the {111} and {220} planes are positive at RT but negative at 400 ℃ and 500 ℃. In contrast, the lattice strain of the {200} plane alternates between positive and negative values across the RT-500 ℃ range. This demonstrates that the {200} plane is most sensitive to intergranular stress. The {311} plane is a representative plane that reflects the macroscopic mechanical response of FCC crystals during quasi-static deformation. It also aligns with the average strain evolution trend obtained from full-pattern Rietveld refinement[31]. In this study, the lattice strains of the {311} plane at RT-500 ℃ are similar in magnitude and remain negative after SHPB compression, as shown in Fig. 6(b). This behavior differs from the discrete distribution characteristics observed for the {111}, {200}, and {220} planes under the three temperature conditions.

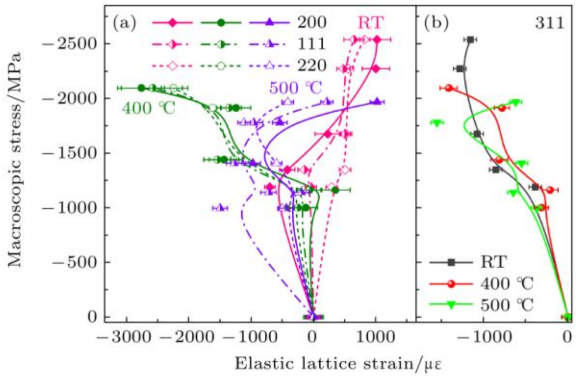

Fig. 6 {*hkl*} lattice strains of GH4738 superalloy measured by RSND at RT-500 ℃: (a) {111}, {200}, and {220} planes; (b) {311} plane. Note that με represents microstrain, with a value of 10^{-6}.

Equation (2) was further employed to convert the lattice constants obtained from full-pattern Rietveld refinement into the average elastic strains of the γ and γ' phases. The results are presented in Figure 7. The data indicate that the elastic strain of the γ' phase increases with increasing external load. In contrast, the elastic strain of the γ phase remains nearly constant. Furthermore, the elastic strain of the γ' phase at room temperature (RT) is lower than that observed at elevated temperatures (400 ℃ and 500 ℃). The average phase strain was calculated by weighting the elastic strains of the γ and γ' phases by their respective volume fractions of 70% and 30%. These results are shown in Figure 8, which also includes the lattice strain of the {311} plane for visual comparison. At RT and 500 ℃, the average phase strains for both the γ and γ' phases are compressive and continue to increase. The magnitude of this increase at 500 ℃ is significantly greater than that at RT. At 400 ℃, the average phase strain initially increases in the tensile direction before reversing to increase in the compressive direction. This condition exhibits the largest strain amplitude among the three temperatures. Moreover, under conditions of significant frozen strain (ε = -0.20—-0.25), the lattice strain of the {311} plane at 400 ℃ continues to increase in compression. Conversely, at RT and 500 ℃, the lattice strain of the {311} plane rebounds toward tension. This behavior demonstrates that the {311} plane generates substantial intergranular stress/strain due to plastic deformation during SHPB dynamic compression. Consequently, it no longer exhibits a consistent response with the macroscopic residual stress (internal stress).

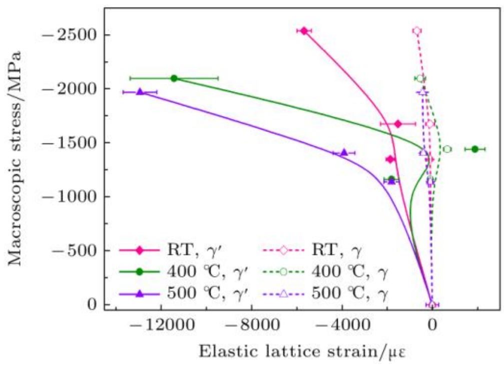

Fig. 7 Averaged elastic strains in the *γ* and *γ′* phases of GH4738 superalloy measured at RT-500 ℃.

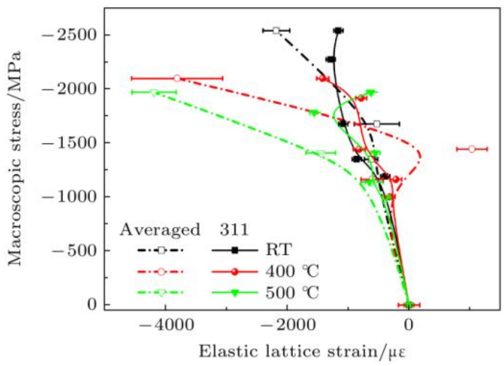

Fig. 8 Averaged phase-specific strains and {311} lattice strains of GH4738 superalloy measured at RT-500 ℃.

3.4 Defect Characteristics

To elucidate the microscopic mechanisms underlying the dynamic compressive deformation behavior of GH4738 alloy under SHPB loading at room temperature (RT), 400 ℃, and 500 ℃, we employed TEM to characterize defect morphologies at a true strain of -0.3 across these three temperatures. The results are presented in Figure 9. Figure 9(a) shows the initial state of the sample, which contains a low density of dislocations and stacking faults due to material processing and specimen preparation. Under RT conditions, as shown in Figure 9(b), plastic deformation generates extensive parallel slip bands and stacking faults. The precipitates exhibit regular morphology, with dislocations piling up around them. In this plastic deformation mode, dominated by co-deformation of the γ and γ' phases, the γ-γ' lattice misfit (red dotted line in Figure 5), {*hkl*} lattice strain (red dotted line in Figure 6), and phase-averaged strain (black dotted line in Figure 8) remain relatively low at RT. At 500 ℃, as illustrated in Figure 9(d), the dislocation density increases sharply, producing abundant dislocation debris. Both dislocation pile-ups and stacking fault density are significantly higher than those observed at RT. Furthermore, the γ' phase exhibits irregular morphology at 500 ℃. This phenomenon may be attributed to temperature-assisted slip and the activation of additional plastic deformation mechanisms within the γ' phase at this temperature[28]. Corresponding to this dislocation configuration, the γ-γ' lattice misfit and phase-averaged strain reach their maximum values. However, the overall {*hkl*} lattice strain is lower than that observed at 400 ℃ (purple and green dotted lines in Figure 6), indicating that intergranular stress is lower than in the 400 ℃ case. Under 400 ℃ conditions, as shown in Figure 9(c), the densities of dislocations and stacking faults are significantly lower than those at RT and 500 ℃, and the precipitates maintain a regular and ordered morphology. The corresponding γ-γ' lattice misfit, {*hkl*} lattice strain, and phase-averaged strain exhibit a reversal trend at a strain of approximately -0.05 (corresponding stress: -1162 MPa), followed by a sharp positive increase. This behavior is indicated by the green dotted lines in Figures 5(b)-(d) and 6(a), and the red dotted line in Figure 8. This suggests that at 400 ℃, dislocation climb dominates within the strain range of -0.05 to -0.10. Consequently, the horizontal γ-γ' lattice misfit decreases while the vertical lattice misfit increases (green dotted lines in Figures 5(c) and (d)). Additionally, the residual strain along the SHPB compression direction transitions toward tensile strain (red dotted line in Figure 8). When the strain exceeds -0.10, dislocation slip becomes dominant. The dislocation multiplication rate approaches the recovery rate, resulting in a slow increase in dislocation density. Compared to RT, the γ-γ' lattice misfit and lattice distortion at 400 ℃ cannot be fully relaxed by an increase in dislocation density. This leads to a continuous increase in {*hkl*} lattice strain, as shown in Figure 6. In contrast, at RT and 500 ℃, the continuous increase in dislocation density (Figures 9(b) and (d)) allows for partial recovery of elastic lattice distortion. Consequently, a rebound phenomenon in {*hkl*} lattice strain occurs at higher strains (ε = -0.20 to -0.25).

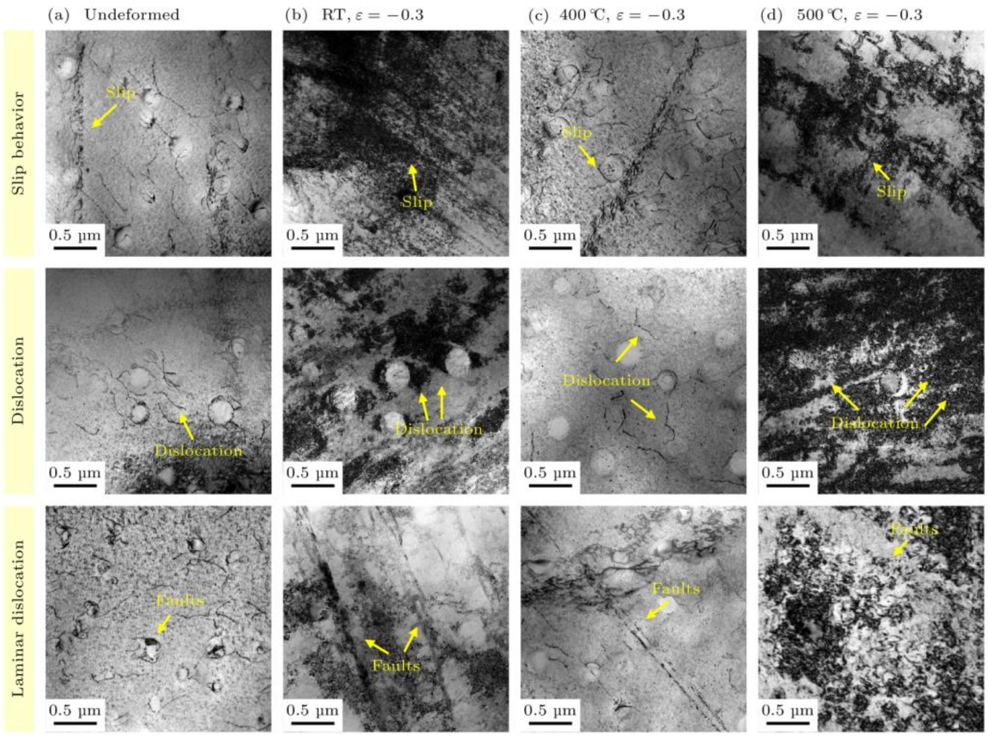

Fig. 9 TEM characterization of defects in GH4738 superalloy in the initial and deformed states at RT-500 ℃: (a) Undeformed; (b) RT, ε = –0.3; (c) 400 ℃, ε = –0.3; (d) 500 ℃, ε = –0.3.

4 Conclusions

This study prepared a series of strain-frozen specimens from SHPB compression tests at high strain rates. We characterized the anisotropic features of GH4738 alloy under high-speed deformation at room temperature (RT) to 500 ℃ from multiscale perspectives, including lattice, grain, phase, and defect levels. We established the correlation between microstructural and defect evolution and microscopic stress/strain. The main conclusions are as follows.

1) At strain rates of 1000—7500 s^{-1} and temperatures from RT to 500 ℃, the yield strength decreases with increasing temperature but increases with increasing strain rate. However, the yield strength drops sharply at 500 ℃ and a strain rate of 7500 s^{-1}.

2) The horizontal lattice misfit is positive and increases with increasing frozen strain. The vertical lattice misfit decreases with increasing frozen strain, transitioning from positive to negative values. At 400 ℃, the lattice misfit fluctuates when the frozen strain ranges from –0.05 to –0.10.

3) The lattice strain values for the {311} plane are similar at RT, 400 ℃, and 500 ℃, and remain negative after SHPB compression. In contrast, the lattice strains for the {111}, {200}, and {220} planes exhibit distinct distribution characteristics across the three temperatures. The {200} plane is the most sensitive to intergranular stress.

4) At RT, plastic deformation is dominated by γ-γ' co-deformation. The defects consist of parallel slip bands and stacking faults. The dislocation networks at the γ/γ' interfaces

effectively relax lattice misfit, resulting in minimal residual lattice strain. At 500 ℃, both γ and γ' phases undergo plastic deformation readily under the thermal field. The dislocation density increases significantly. The dislocation networks at the γ/γ' interfaces cannot compensate for the lattice distortion caused by defect proliferation. Consequently, both lattice misfit and residual lattice strain remain high. At 400 ℃, alternating dominance of dislocation climb and glide causes fluctuations in lattice misfit and residual lattice strain. Due to the slow increase in dislocation density, the {*hkl*} lattice strain continues to rise. This behavior differs from that at RT and 500 ℃, where increased dislocation density leads to partial recovery of elastic lattice distortion. At higher strains (ε = –0.20 to –0.25), the {*hkl*} lattice strain even exhibits rebound characteristics.

5) Future work should prioritize SHPB testing at temperatures above 500 ℃ and strain rates exceeding 3000 s^{-1}, along with corresponding neutron diffraction microstructural characterization. These efforts are essential to comprehensively reveal the dynamic damage mechanisms of nickel-based superalloys.

References

[1] Shi C, Zhong Z 2010 *Acta Metall. Sin.* **46** 1281

[2] Pollock T M, Tin S 2006 *J. Propul. Power* **22** 361

[3] Yang J J, Li H J, Gao T, Zhang C S, Xia Y H, Li J, Huang C Q, Zhong S Y, Sun G G 2024 *J. Alloy. Compd.* **977** 173382

[4] Jaladurgam N R, Li H, Kelleher J, Persson C, Steuwer A, Colliander M H 2020 *Acta Mater.* **183** 182

[5] Daymond M R, Preuss M, Clausen B 2007 *Acta Mater.* **55** 3089

[6] Francis E M, Grant B M B, Fonseca J Q D, Phillips P J, Mills M J, Daymond M R, Preuss M 2014 *Acta Mater.* **74** 18

[7] Li H, Larsson F, Colliander M H, Ekh M 2021 *Mater. Sci. Eng. A* **799** 140325

[8] Wang Y D, Li R G, Nie Z H, Li S L 2022 *Chin. J. Eng.* **44** 676

[9] Sun G A, Chen B, Wu E D, Li W H, Zhang G, Wang X L, Ji V, Pirling T, Hughes D 2011 *Acta Phys. Sin.* **60** 086102

[10] Coakley J, Lass E A, Ma D, Frost M, Seidman D N, Dunand D C, Stone H J 2017 *Scripta Mater.* **134** 110

[11] Sieborger D, Brehm H, Wunderlich F, Moller D, Glatzel U 2021 *Int. J. Mater. Res.* **92** 58

[12] Huang S, An K, Gao Y, Suzuki A 2018 *Metall. Mater. Trans. A* **49A** 740

[13] Yan Z R, Tan Q, Gao Y, Rong Y, Qin H L, Bi Z N, Gong W, Harjo S, Wang Y

D 2025 *Mater. Sci. Eng. A* **945** 148976

[14] Liu Y B, Yan Z R, Gao Y, Li Y, Gan B, Harjo S, Gong W, Kawasaki T, Li S L, Wang Y D 2025 *Microstructures* **5** 2025096

[15] Beese A M, Wang Z, Stoica A D, Ma D 2018 *Nat. Commun.* **9** 2083

[16] Aba-Perea P E, Withers P J, Pirling T, Paradowska A, Ma D, Preuss M 2019 *Metall. Mater. Trans. A* **50A** 3555

[17] Liu Z X, Zhao Z Y, Zheng T, Mu J, Xie G, Zhang J, He L H, Wang Y D 2024 *Acta Mater.* **281** 120430

[18] D'Souza N, Kelleher J, Kabra S, Panwisawas C 2017 *Mater. Sci. Eng. A* **681** 32

[19] Yan Z R, Srikakulapu K, Gao Y, Qin H L, Rong Y, Bi Z N, Xie Q G, An K, Wang Y D, Tan Q 2023 *Scripta Mater.* **236** 115665

[20] Kumar S S S, Raghu T, Bhattacharjee P P, Rao G A, Borah U 2016 *J. Alloy. Compd.* **681** 28

[21] Janeiro I S, Franchet J, Cormier J, Bozzolo N 2023 *Metall. Mater. Trans. A* **54A** 2052

[22] Zhang L, Townsend D 2024 *Mater. Lett.* **358** 135822

[23] Parthasarathy T A, Porter W J, Buchanan D J, John R 2016 *Mater. Sci. Eng. A* **661** 247

[24] Horikoshi S, Yanagida A, Yanagimoto J 2020 *Isij Int.* **60** 2905

[25] Zhang J Y, Xu B, Tariq N U H, Sun M, Li D, Li Y 2020 *J. Mater. Sci. Technol.* **40** 54

[26] Xie L, Chen X P, Fang L M, Sun G G, Xie C M, Chen B, Li H, Ulyanov V A, Solovei V A, Kolkhidashvili M R, Bulkin A P, Kalinin S I, Wang Y, Wang X L 2019 *Nucl. Instrum. Meth. A* **915** 31

[27] Li J, Wang H, Sun G G, Chen B, Chen Y Z, Pang B B, Zhang Y, Wang Y, Zhang C S, Gong J, Liu Y G 2015 *Nucl. Instrum. Meth. A* **783** 76

[28] Li H, Ekh M, Colliander M H, Larsson F 2018 *Int. J. Plasticity* **110** 248

[29] Sabine T M 1977 *J. Appl. Crystallogr.* **10** 277

[30] Ata-Allah S S, Balagurov A M, Hashhash A, Bobrikov A, Hamdy S 2016 *Physica B* **481** 118

[31] Ezeilo A N, Webster G A, Webster P J, Wang X 1992 *Physica B* **180-181** 1044